Why the observed spin evolution of older-than-solar like stars might not require a dynamo mode change

Ketevan Kotoroshvili [1,2]★, Eric G. Blackman[1,2]†,James E. Owen[3]‡
[1]Department of Physics and Astronomy, University of Rochester, Rochester NY 14627
[2]Laboratory for Laser Energetics, University of Rochester, Rochester, NY 14623, USA
[3]Astrophysics Group, Department of Physics, Imperial College London, Prince Consort Rd, London SW7 2AZ, UK

13 January 2023

ABSTRACT

The spin evolution of main sequence stars has long been of interest for basic stellar evolution, stellar aging, stellar activity, and consequent influence on companion planets. Observations of older than solar late-type main-sequence stars have been interpreted to imply that a change from a dipole-dominated magnetic field to one with more prominent higher multipoles might be necessary to account for the data. The spin-down models that lead to this inference are essentially tuned to the sun. Here we take a different approach which considers individual stars as fixed points rather than just the Sun. We use a time-dependent theoretical model to solve for the spin evolution of low-mass main-sequence stars that includes a Parker-type wind and a time-evolving magnetic field coupled to the spin. Because the wind is exponentially sensitive to the stellar mass over radius and the coronal base temperature, the use of each observed star as a separate fixed point is more appropriate and, in turn, produces a set of solution curves that produces a solution envelope rather than a simple line. This envelope of solution curves, unlike a single line fit, is consistent with the data and does not unambiguously require a modal transition in the magnetic field to explain it. Also, the theoretical envelope does somewhat better track the older star data when thermal conduction is a more dominant player in the corona.

Key words: stars: late-type – stars: low-mass – stars: solar-type – stars: mass-loss.

1 INTRODUCTION

Understanding the coupled spin-activity evolution of stars is of interest both for the basic physics of rotating stellar evolution and stellar activity, for determining stellar ages via gyrochronology, and for quantifying the influence of stellar activity on companion planetary atmospheres. Predicting the spin evolution of main sequence stars and the associated activity ultimately requires an accurate model for the coupled evolution of their magnetic fields, their spin, their activity and mass loss.

Until recently the standard period-age evolution for main sequence solar-like FGK stars has been divided into two regimes, saturated and unsaturated. The empirically determined transition between them occurs at $\tilde{Ro} \sim 0.13$, where the Rossby number $\tilde{Ro}$ is defined as $\tilde{Ro} = P/\tau_c$, with P being the star's rotation period and τ_c the stellar model-inferred convective turnover time (Wright et al. 2011; Reiners et al. 2014). Very young, X-ray luminous stars are in the saturated regime where their X-ray to bolometric luminosity ratio is nearly independent of rotation rate. Older stars are in the unsaturated regime for which the period age relation has been traditionally characterized by the empirical Skumanich law (Skumanich 1972). Recently however, for a sub-population of stars older than the sun, the spin-down rate has been purported to be slower than that of the Skumanich law(Skumanich 1972) and slower than that predicted by some standard spin-down models with a fixed magnetic field geometry (Matt et al. 2012; Reiners & Mohanty 2012; van Saders & Pinsonneault 2013; Gallet & Bouvier 2013; Matt et al. 2015; van Saders et al. 2016). This has led to the suggestion that dynamos in these stars may be incurring a state transition from dipole to one in which the field is dominated by higher multipoles that less effectively remove angular momentum (van Saders et al. 2016). Such a transition would then warrant a theoretical explanation.

The importance of this potential transition warrants further investigation to assess whether it is unambiguous. In particular, how precise are the predictions of spin evolution from current theoretical models that invoke no dynamo transition, and how are these models used to obtain a predicted envelope of spin-period evolution bounds for the evolution of a population of stars similar to, but not identical to, the Sun?

To address this, we study the time evolution of the rotation period for older-than-solar late-type stars using an example theoretical model for the coupled time evolution of the X-ray luminosity, magnetic field strength, mass loss and rotation. Importantly, the observed data for each star provides boundary conditions needed to solve the system of equations for each specific star. We do not assume that each star is an identical twin to the sun. This distinction proves to be important in limiting the precision of what can be inferred and the robustness of whether the observations definitively reveal the need for a dynamo transition in each star.

In Section 2, we summarize the minimalist theoretical model that

★ kkotoras@ur.rochester.edu
† eric.blackman@rochester.edu
‡ james.owen@imperial.ac.uk

couples the time evolution of X-ray luminosity, rotation, magnetic field and mass loss (Blackman & Owen 2016). In Subsection 2.3 we provide expressions for X-ray luminosity and mass loss as a function of the X-ray coronal temperature for cases when thermal conduction is dominant and when thermal conduction can be ignored. Thermal conduction can reduce the hot gas supply to the wind, lowering its ability to spin down the star, but also keeps the magnetic field stronger longer which would exacerbate spin down. The net effect of this competition has yet to be quantified. In Section 3 we obtain solutions for the time evolution of the rotation period of each individual star in a sample of old stars with observed spins and ages, using their observed stellar properties as fixed point boundary conditions for the solutions. We find that even the small variations in observed properties (e.g. magnetic field, mass, radius) between solar-like stars, makes fitting an evolution model to a single star like the Sun not sufficiently representative of the population to identify that the population as a whole is incurring a dynamo transition. We conclude in Section 4 and address some broader implications for comparing theory and observation.

2 PHYSICAL MODEL AND EQUATIONS

Main sequence low-mass stars spin down as a consequence of their magnetized stellar winds (Parker 1958; Schatzman 1962; Weber & Davis 1967; Mestel 1968). F, G , K and M stars with masses in the range $0.35M_\odot < M < 1.5M_\odot$ have a convective zone surrounded by a radiative zone and are in that respect potentially most solar-like with respect to their dynamos (Parker 1955; Steenbeck & Krause 1969). The magnetic field anchors the stellar wind to the surface of the star, forcing it to co-rotate up to the Alfvén radius, so angular momentum is lost from the star. As a result, the reduced angular momentum means reduced free energy available for the dynamo, and the magnetic field and X-ray luminosity also decrease. Therefore the strength of the magnetic field at the surface, the rate of angular momentum loss, X-ray luminosity and the rotation period are fundamentally linked (Kawaler 1988).

Here we use and adapt a minimalist holistic model for this coupled time evolution of X-ray luminosity, mass loss, rotation and magnetic field strength (Blackman & Owen 2016) to explain the flattening in the observed period–age relation for older stars than the sun. In this model, some fraction of dynamo-generated magnetic field lines are considered open, allowing stellar wind to remove angular momentum, while some fraction of field lines are considered closed, sourcing the thermal X-ray emission. The magnetic field expression is based on a dynamo saturation model in a regime where the total saturated field strength depends on the rotation rate The dynamo-produced magnetic field is then mutually evolving with the spin evolution of low-mass main-sequence stars in this slow rotator regime.

In this section, we briefly summarize the minimalist theoretical model that couples the time evolution of the aforementioned stellar properties, discuss the main ingredients of the model, and point out a few numerical coefficient corrections to previous work. We also apply the formalism for stars other than the Sun and use the properties of each individual star for which we have observed data as a boundary condition for respective solutions. The importance of this as it pertains to making the theoretical prediction of spin-down with age an "envelope" rather than a "single line" will be exemplified and emphasized later in the paper. We provide only the streamlined set of resulting equations here, and the detailed derivations of the original model equations on which our revised derivations are based can be found in Blackman & Owen (2016).

2.1 Saturated magnetic field and X-ray luminosity

The dynamo-produced magnetic fields are estimated (Blackman & Thomas 2015; Blackman & Owen 2016) by: (1) using a generalized correlation time for dynamos that equals the convection time (τ_c) for slow rotators and becomes proportional to the rotation time for fast rotators and (2) using a dynamo saturation model, based on the combination of magnetic helicity evolution and loss of magnetic field by magnetic buoyancy (Blackman & Field 2002; Blackman & Brandenburg 2003). In the slow-rotator regime of interest, the field saturation depends on the rotation rate, but the exact field saturation model is less important than the fact that there remains a spin dependence of the field strength and that the saturation time (of order cycle period) is short compared to the Gyr time scales of secular evolution we are interested in. This results in the expression for normalized surface radial magnetic field:

$$b_r \equiv \frac{B_{r*}(t)}{B_{r,*n}} = g_L(t)\left(\frac{s}{s_*}\right)^{1/6}\sqrt{\frac{1+s_*\tilde{R}o_*}{1+s\tilde{R}o}}, \tag{1}$$

where $B_{r,*n}$ is present-day radial magnetic field value for each star (here n indicates "now") and $g_L(t) = \left(\frac{1}{1.4-0.4t}\right)^{\frac{\lambda-1}{4}}$. This factor approximates the fusion-driven increase in the bolometric luminosity with time t in units of solar age from solar models (Gough 1981, e.g.), and deviates from unity only if $\mathcal{L}_{bol}$ evolves. We crudely apply the same approximation for other solar-like stars scaled in terms of their age. More detailed empirical fits for each stellar model could be inferred but this is beyond the level of precision required for present purposes. . Here s is a shear parameter defined as $|\Omega_0 - \Omega(r_c, \theta_s)| = \Omega_0/s$, where Ω is surface rotational speed; θ_s is a fiducial polar angle; r_s is a fiducial radius in the convective zone and λ is a parameter representing the power law dependence of the magnetic starspot area covering fraction Θ on X-ray luminosity $\mathcal{L}_X$, namely $\Theta \propto \mathcal{L}_X^\lambda$. In our case, we take $\lambda = 1/3$, consistent with the range inferred from observations of star spot covering fractions (Nichols-Fleming & Blackman 2020) and we fix the shear parameter at $s = 8.3$, because the transition from the saturated to the unsaturated regime of X-ray luminosity was best matched theoretically with this value (Blackman & Thomas 2015; Blackman & Owen 2016). In practice, this has to be determined with detailed calculations, but the specific value does not affect the overall message of the present paper as our focus is on the unsaturated regime where the shear term contribution to the correlation time is small.

The estimated X-ray luminosity derived in Blackman & Thomas (2015) is the product of the magnetic energy flux, averaged over the change over a stellar cycle for sun-like stars (Peres et al. 2000), times the surface area through which the magnetic field penetrates the photosphere. The result is

$$\mathcal{L}_x = \mathcal{K}\mathcal{L}_{mag} \simeq \mathcal{K}\frac{2}{3}\left(\frac{B_\phi^2}{8\pi}\right)^2\frac{\Theta r_c^2}{\rho v}, \tag{2}$$

where ρ is a density and v is a turbulent convective velocity; and $\mathcal{K}$ defines how much magnetic energy goes to X-ray luminosity. In (Blackman & Owen 2016) $\mathcal{K}$ was approximated as $1/2$ based on the coronal equilibrium solution when conduction is unimportant. We find this is also an acceptable approximation when conduction dominates so we adopt it. This leads to the relation between X-ray luminosity and radial magnetic field (Blackman & Owen (2016)):

$$l_x \equiv \frac{1}{1.4-0.4t}\left(\frac{s}{s_*}\right)^{\frac{2}{3(1-\lambda)}}\left(\frac{1+s_*\tilde{R}o_*}{1+s\tilde{R}o}\right)^{\frac{2}{1-\lambda}} = b_r^{\frac{4}{1-\lambda}}. \tag{3}$$

where $\tilde{R}o_*$ is the Rossby number for each individual star. For the sun $\tilde{R}o \sim 2$ Blackman & Thomas (2015).

2.2 Angular velocity evolution

Blackman & Owen (2016) considered angular momentum loss by the stellar wind in the equatorial plane and used the (Weber & Davis (1967)) model to find the surface toroidal magnetic field and the equation for angular velocity. Following derivations in Weber & Davis (1967), Lamers & Cassinelli (1999) and Blackman & Owen (2016) for the Alfvén radius we have

$$\frac{r_A}{r_*} = \left(1 - \frac{r_* B_{r*} B_{\phi*}}{\dot{M}\Omega_*}\right)^{1/2} = \left(1 + \frac{r_* |B_{r*}||B_{\phi*}|}{\dot{M}\Omega_*}\right)^{1/2}, \tag{4}$$

where compared to the same equation in Blackman & Owen (2016), we emphasize that there is a positive sign when absolute values are used because of the opposite signs of $B_{\phi*}$ and B_{r*}.

Separate equations for $\frac{r_A}{r_*}$ and toroidal magnetic field are:

$$\frac{r_A}{r_*} = \frac{b_{r*}}{\dot{m}^{1/2}\tilde{u}_A^{1/2}} \frac{r_* B_{r,*n}}{\dot{M}_{*n}^{1/2} u_{A,*n}^{1/2}}, \tag{5}$$

$$b_{\phi*} \equiv \frac{B_{\phi*}(t)}{B_{\phi,*n}} = -\frac{\dot{m}\omega_*}{b_{r_*}} \frac{M_{*n}\Omega_{*n}}{r_* B_{\phi,*n} B_{r,*n}} \left[\frac{r_A^2}{r_*^2} - 1\right], \tag{6}$$

where $B_{\phi,*n}$ is a present-day toroidal magnetic field value for each star; $\dot{m}$ is a mass loss derived later (see equations (17) and (18) for regime I and regime II respectively); $\omega_*(t) = \Omega(t)/\Omega_{*n}$, where Ω_{*n} represents the present day value of angular velocity for each individual star. For the Sun, $\Omega_{*n} = \Omega_\odot = 2.97 \cdot 10^{-6}/s^2$, $B_{\phi,*n} = B_{\phi\odot} = 1.56 \cdot 10^{-2} G$, $B_{r,*n} = B_{r\odot} = 2G$. For other stars, the corresponding values in Table 1 will be used. In equation (5), $\tilde{u}_A(t)$ is the normalized Alfvén speed given by

$$\tilde{u}_A(t) \equiv \frac{u_A}{u_{A,*n}} = \sqrt{\frac{T_*}{T_{*n}}} \frac{W_k[-D(r_A)]}{W_k[-D(r_{A,*n})]}, \tag{7}$$

where T_* is the coronal X-ray temperature and T_{*n} is the coronal X-ray temperature at present time (now) for each specific star. $W_k[-D(r_A)]$ is the Lambert W function for Parker wind solutions $k = 0$ for $r \leq r_s$ and $k = -1$ for $r \geq r_s$ (Cranmer 2004) and

$$D(r_A) = \left(\frac{r_A}{r_s}\right)^{-4} \exp\left[4\left(1 - \frac{r_s}{r_A}\right) - 1\right]. \tag{8}$$

The sonic radius is given by

$$\frac{r_s}{r_*} = \frac{GM}{2c_s^2 r_*} \tag{9}$$

with isothermal sound speed $c_s \propto T^{1/2}$.

The evolution of stellar angular velocity in dimensionless form is given by

$$\frac{d\omega_*}{d\tau} \equiv -\omega_* \frac{q b_r^2}{m\tilde{u}_A} \frac{B_{r,*n}^2 \tau_{*n}}{M_{*n} u_{A,*n}}, \tag{10}$$

where $\tau_\odot$ is present-day solar age; q is the inertial parameter, that depends on internal angular momentum transport and defines what fraction of the star contributes to the spin-down (and corrected a typo on the right of equation (41) of Blackman & Owen (2016) which had residual factor of $\Omega_\odot$). We use $q = 1$ for all stars, which indicates a conventional assumption that the field is coupled to the moment of inertia of the full stellar mass. This could in principle be violated if the field were not anchored sufficiently deeply and angular momentum transport within the star was inefficient.

2.3 Coronal Equilibrium: relation between $\mathcal{L}_x$, $\dot{M}$ and T_0

The above equations show that X-ray luminosity, dynamo-produced magnetic field and angular velocity are all coupled. To determine how all of these quantities are connected to the mass loss rate, we follow the procedure of Blackman & Owen (2016) but since that paper focused on younger-than-solar stars, here we study both younger and older stars and generalize the equations accordingly.

Magnetic fields are the source of input energy to the corona in our model, which is then distributed into either winds, x-rays, or lost to the photosphere by thermal conduction. Equilibrium is established between the sinks of mass loss, X-ray radiation and conduction over time scales short compared to spin-down time scales and can be used to determine the dominant sinks of the magnetic energy flux.

According to Hearn (1975), for a given coronal base pressure, there is an average coronal temperature that minimizes energy loss. The minimum coronal flux condition is given by

$$\frac{\partial}{\partial T}(F_{W1} + F_c + F_x) = \frac{\partial}{\partial T} F_B = 0, \tag{11}$$

where F_B is the flux of magnetic energy sourced into the coronal base and F_{W1}, F_c, F_x are respectively the wind flux, conductive loss, and the radiative (X-ray) loss, from the one density scale height region above the chromosphere.

The expression for coronal energy loss in the stellar wind is given by

$$F_{W1} = 3.1 \times 10^6 p_0 \tilde{T}_*^{1/2} e^{3.9\frac{m_*}{r_*}\left(1-\frac{1}{\tilde{T}_*}\right)} \frac{\text{erg}}{cm^2 \cdot s}, \tag{12}$$

where we used the isothermal Parker wind solution (Parker 1955) along with the assumption of large-scale magnetic fields being approximately radial out to the Alfvén radius (r_A). Here $\tilde{T}_* = \frac{T_*}{T_*'}$ is a dimensionless temperature with a different normalization parameter T_*' for each star; $m_* = \frac{M}{M_{*n}}$ and $r_* = \frac{R_0}{R_{*n}}$, where M_{*n} and R_{*n} represent a specific individual stellar mass and radius. Normalizing stellar parameters to individual stars, we then have $m_* = r_* = 1$. We also use $p_0 \sim \rho_0 c_s^2$ where the subscript 0 indicates values at the coronal base and we use CGS units for p_0.

For the X-ray radiation flux, we have

$$F_x = 1.24 \times 10^6 \frac{p_0^2}{\tilde{T}_*^{5/3}} \frac{r_*^2}{m_*} \frac{\text{erg}}{cm^2 \cdot s}, \tag{13}$$

For the conductive loss,

$$F_c = 4.26 \times 10^6 p_0 \tilde{T}_*^{3/4} \frac{\tilde{\Theta}}{4\pi} \frac{\text{erg}}{cm^2 \cdot s}, \tag{14}$$

where the solid angle correction fraction $\frac{\tilde{\Theta}}{4\pi} \leq 1$ arises because conduction down from the corona is assumed to be non-negligible only along the fraction of the solid angle covered with field lines perpendicular to the surface.

There is a monotonic relation between the base pressure of the corona and the energy density at coronal equilibrium, and all three energy losses increase with the base coronal pressure. The above equations lead to an equilibrium pressure (with corrected numerical coefficients in the first and third term, as well as the corrected factor of $\frac{m_*}{r_*}$ in the last term compared to Blackman & Owen (2016))

$$\begin{aligned} p_0 = \frac{m_*}{r_*^2} 0.12 \tilde{\Theta} \tilde{T}_{0*}^{\frac{29}{12}} + \frac{m_*}{r_*^2} 0.75 \tilde{T}_{0*}^{\frac{13}{6}} e^{3.9\frac{m_*}{r_*}\left(1-\frac{1}{\tilde{T}_{0*}}\right)} \\ + \frac{m_*^2}{r_*^3} 5.85 \tilde{T}_{0*}^{\frac{7}{6}} e^{3.9\frac{m_*}{r_*}\left(1-\frac{1}{\tilde{T}_{0*}}\right)}, \end{aligned} \tag{15}$$

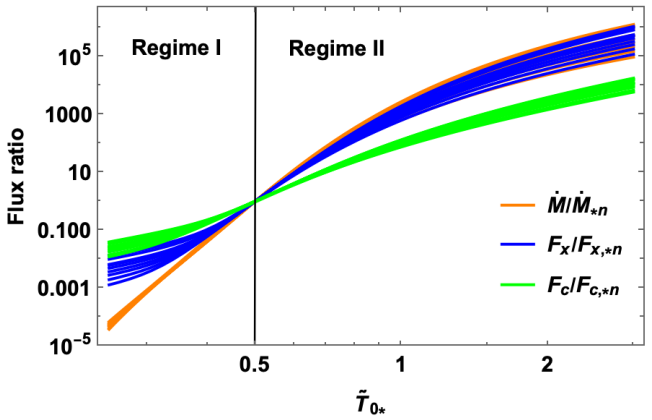

Figure 1. Normalized energy fluxes of X-rays $\frac{F_X}{F_{X,*n}}$ (blue); thermal conduction $\frac{F_C}{F_{C,*n}}$ (green);, and mass outflow $\frac{\dot{M}}{\dot{M}_{*n}}$ (orange) are shown for each individual star of Table 1. Similar plots were shown in Blackman & Owen (2016) but only for the sun. The y-axis is in units of individual stellar values for each quantity and the unobserved equilibrium temperature T_{0*} for each star is normalized such that a transition between the dominance and sub-dominance of thermal conduction occurs at dimensionless $\tilde{T}_{0*} = 0.5$. In regime I, ($\tilde{T}_{0*} < 0.5$), thermal conduction is dominant, but it is subdominant in regime II ($\tilde{T}_{0*} > 0.5$), where $l_X \simeq \dot{m}$. Regime I corresponds to older and regime II to younger phases of the main sequence for a given star. The envelope of these curves for the different stars produces the bands of color for each energy flux.

where $\tilde{T}_{0*} = \frac{T_{0*}}{T'_*}$, T_{0*} is the coronal temperature at equilibrium for each specific star. For the present solar coronal temperature we take $T_{0,*n} \sim T_\odot \sim 1.5 \times 10^6 K$ and for T'_* we used $T'_* = T'_\odot = 3 \times 10^6 K$, so that at $\tilde{T}_{0*} = 0.5$, $l_X = \frac{\mathcal{L}_X}{\mathcal{L}_{X,*n}} = 1$ and $\dot{m} = \frac{\dot{M}}{\dot{M}_{*n}} = 1$.

Fig.1 shows radiation, conduction and total coronal wind fluxes $\frac{F_X}{F_{X,*n}}, \frac{F_C}{F_{C,*n}}, \dot{m} = \frac{F_{W1}\tilde{T}_{0,*n}}{F_{W1,*n}\tilde{T}_{0*}}$ as a function of equilibrium temperature, where $\tilde{T}_{0,*n}$ is the coronal temperature at present time for sun-like stars. All the quantities (y-axis) and the equilibrium temperature (x-axis) are normalized to their respective stellar values for an individual star. We define Regime I as the lifetime phase of a star for which thermal conduction flux dominates the outflow flux and Regime II when the reverse is true. This occurs at a different coronal equilibrium temperature T_{0*} specific to each star. We then define the transition to occur at the same arbitrary dimensionless value of 0.5 for each star such that $\tilde{T}_{0*} < 0.5$ corresponds to regime I and $\tilde{T}_{0*} > 0.5$ corresponds to regime II. The vertical line at $\tilde{T}_{0*} = 0.5$ represents the transition between the two regimes which have different relations between X-ray luminosity and mass loss.

2.3.1 Regime I (conduction dominated)

In this regime, which generally corresponds to the spun-down older main-sequence phase of a given star, the first term of equation (15) dominates. Consequently, the normalized value for the X-ray luminosity is $l_X = \frac{\mathcal{L}_X}{\mathcal{L}_{X,*n}} = \frac{F_X}{F_{X,*n}}$, which, for each star can be written

$$l_X \simeq \left(\frac{\tilde{T}_{0*}}{\tilde{T}_{0,*n}}\right)^{\frac{19}{6}}. \tag{16}$$

The normalized mass loss is $\dot{m} = \frac{\dot{M}}{\dot{M}_\odot}$

$$\dot{m} \simeq \left(\frac{\tilde{T}_{0*}}{\tilde{T}_{0,*n}}\right)^{\frac{23}{12}} e^{\frac{3.9}{\tilde{T}_{0,*n}}\frac{m_*}{r_*}\left(1-\frac{\tilde{T}_{0,*n}}{\tilde{T}_{0*}}\right)}, \tag{17}$$

which couples with the three other stellar properties discussed above.

2.3.2 Regime II (no conduction)

In this regime, which generally corresponds to the younger, faster-rotating phase of a given star, the second term on the right of equation (15) dominates, which is the outflow flux term. So for l_X and $\dot{m}$ we have (Blackman & Owen 2016)

$$l_X \simeq \exp\left[\ln(\tilde{T}_{0*}) + \frac{7.8}{\tilde{T}_{0*}}\frac{m_*}{r_*}\left(\frac{\tilde{T}_{0*}}{\tilde{T}_{0,*n}} - 1\right)\right] \simeq \dot{m}. \tag{18}$$

3 TIME-EVOLUTION OF ROTATION PERIOD

We numerically solved the four equations (3), (6), (10) and (17) or (18) respectively for regimes I and II, along with equations (5) and (7) for the spin evolution. Importantly, we solved these equations for individual stars, using measured stellar properties as a fixed point (boundary condition) corresponding to the observations of that particular star. The set of solutions comprises an envelope of these individual curves.

3.1 Solutions and comparison to data

Data Table 1 shows the properties of the G-type and F-type stars available for the study. Most of the G stars come from a sample from 21 Kepler with asteroseismology determined ages and measured rotation rates, with effective temperatures between 5700-5900 K (van Saders et al. 2016; Creevey, O. L. et al. 2017). In addition, we include the stars 18 Sco and α Cen A with less precisely measured parameters (van Saders et al. (2016); Metcalfe et al. (2022) and references therein)). Also, we have included a few stars with measured surface magnetic fields and Zeeman Doppler image inferred chromospheric rotation periods from the Bcool project magnetic survey (Marsden et al. 2014). Note that, compared to the Kepler sample, the Bcool survey does not provide precise photosphere rotational periods; however, it provides more precise measurements for magnetic fields. We will present spin evolution solutions for stars 1-10 from this data table for both regimes. The other data points are only for comparison to solutions.

Fig. 2 shows the time evolution of the rotation period for individual stars. The top panel shows solutions for regime I, where energy loss due to conduction is dominant and stellar wind energy loss is very low. The bottom panel shows solutions for regime II, where conduction is negligible, and the X-ray energy losses equal that of the stellar wind. For most stars plotted, we chose the coronal temperature[1] as $\tilde{T}_{0,*n} = \frac{1}{2.4}$ for regime I and $\tilde{T}_{0,*n} = \frac{1}{1.6}$ for regime II solutions. These values correspond to the equilibrium temperatures for the solar minimum and maximum (Blackman & Owen 2016; Johnstone et al. 2015). Overall choosing a different value for $\tilde{T}_{0,*n}$ for both regimes does change the respective slopes of the solutions, but the ranges chosen are consistent with bounds on observed stellar data Johnstone et al. (2015). If we knew the present X-ray temperature,

[1] For stars 2 and 10 form Table 1 we have used $\tilde{T}_{0,*n} = \frac{1}{2.1}$ for regime I solutions.

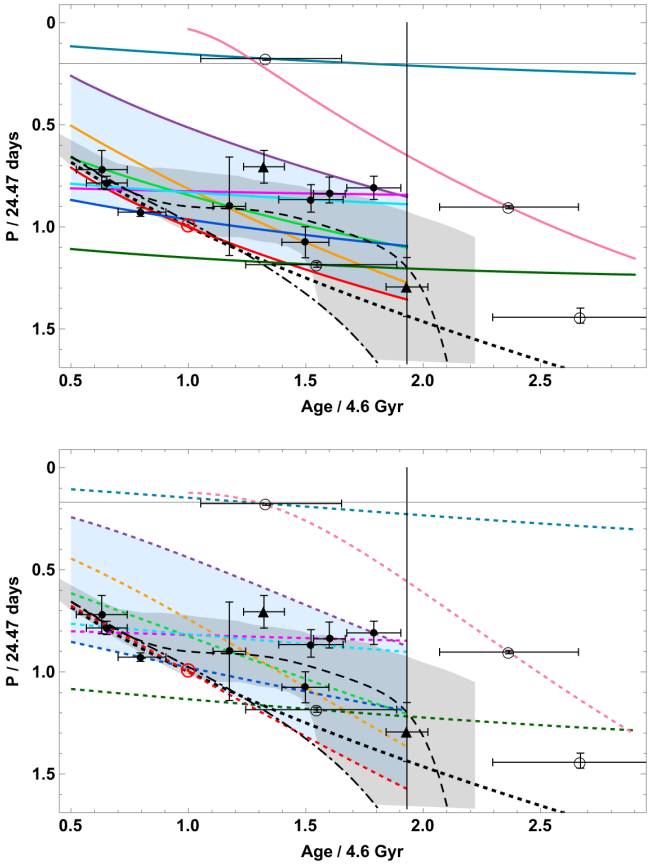

Figure 2. The two panels show envelopes of solution curves for the time evolution of the rotation period, where each observed star is a fixed point on the individual curve. Panel a and b correspond to the regime I and regime II solutions, where the y and x-axis are normalized to solar period and age. Data points and boundary conditions used to find individual solution curves are given in Table 1. Corresponding solutions for row numbers therein are color-coded as 1 - red, 2 - purple, 3 - orange, 4 - green, 5 - magenta, 6 - cyan, 7 - blue, 8 - dark green, 9 - dark cyan and 10 - pink. Open circles correspond to data points from the Bcool project magnetic survey (respectively 8, 9, 10 and 13 from Table 1). (Marsden et al. 2014). The Sun is marked as red ⊙. Triangles represent a star transitioning from the main-sequence to the subgiant phase and a subgiant (respectively 14 and 15 from Table 1). The vertical line represents the cutoff before the subgiant phase for the stars 1-7 in Table 1. The blue-shaded region represents the envelope of solutions for all the stars except the ones with large uncertainties in age from the Bcool project. Both regime I and regime II solutions are compared with the Skumanich law (black dotted line), a standard rotational evolution model (black dot-dashed line) (van Saders et al. 2016), a modified rotational evolution model (black dashed line) and the gray shaded region (Metcalfe & van Saders 2017) that represents the expected dispersion due to different masses, metallicities and effective temperatures between 5600-5900 K.

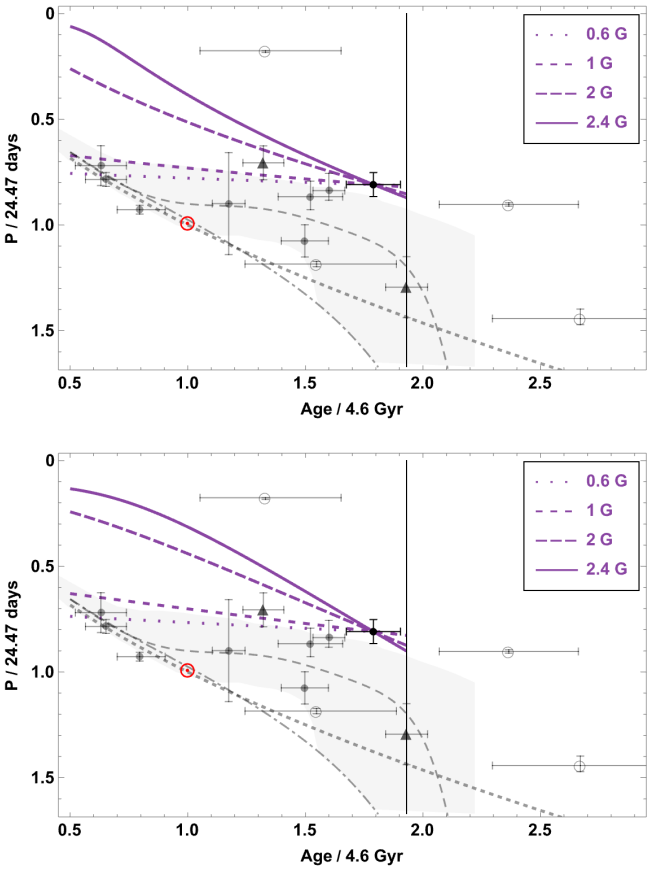

Figure 3. Panels a and b represent the solutions for the time evolution of the rotational period (purple) for one specific star (star 2 from the Table 1) to demonstrate the sensitivity of our solutions to magnetic field strength. These plots show a significant spread for different magnetic field strength normalization values for both regimes I and II. Values used for the magnetic field from bottom to top are B_p = 0.6 G, 1 G, 2 G, 2.4 G, respectively. Data points, black curves (dashed, dotted, dot-dashed) and shaded area have the same meaning as in Fig 2. The vertical line represents the cutoff before the subgiant phase for the stars 1-7 in Table 1.

this would pin down whether a given star is presently in regime I or regime II, and which solution to use. Instead, we compare the consequences of time evolution solutions from either regime for a given star. We find that the implications are not that sensitive to knowing the X-ray temperature over the bounded range because either regime's solutions ultimately lead to our same main conclusions.

Both panels of Fig. 2 also show the modified Skumanich law (Mamajek 2014) $P = t^{0.55}$ and a standard rotational evolution model (van Saders & Pinsonneault 2013; van Saders et al. 2016). Regime I solutions have decreasing slopes as does the empirical Skumanich law, which captures the data trend quite well. Regime II solutions have increasing slopes as does the rotational evolution model used by van Saders et al. (2016), but our solutions comprise an envelope of curves, each passing through a specific star. This envelope is consistent with the observed period-age relation data. In Fig. 2 blue shaded region corresponds to an envelope of solutions for stars with a more precisely measured rotation period and age. It shows that even without including stars from Bcool project this blue-shaded envelope covers the region with the most stars. We include the subgiant star data points on the plot (14 an 15 form Table. 1) we do not show their evolution solutions because we are focusing on main sequence stars only and whether the main sequence stars themselves exhibit a spindown transition. van Saders et al. (2016) does include the subgiant points in their data fitting, and this strongly affects the shape of their shaded area, which rises at late times.

Observations do not provide accurate Rossby numbers for stars 2-7 or magnetic fields for stars 2-4. Since these stars are similar to the sun in other respects, for lack of a better option, we simply assume that these quantities are comparable to solar values. Since the magnetic field is the agent of energy transport into the corona, our solutions are quite sensitive to magnetic field strength. To exemplify this we present solutions for different magnetic field strengths in Fig. 3 for a star without a measured magnetic field. The top panel shows solutions

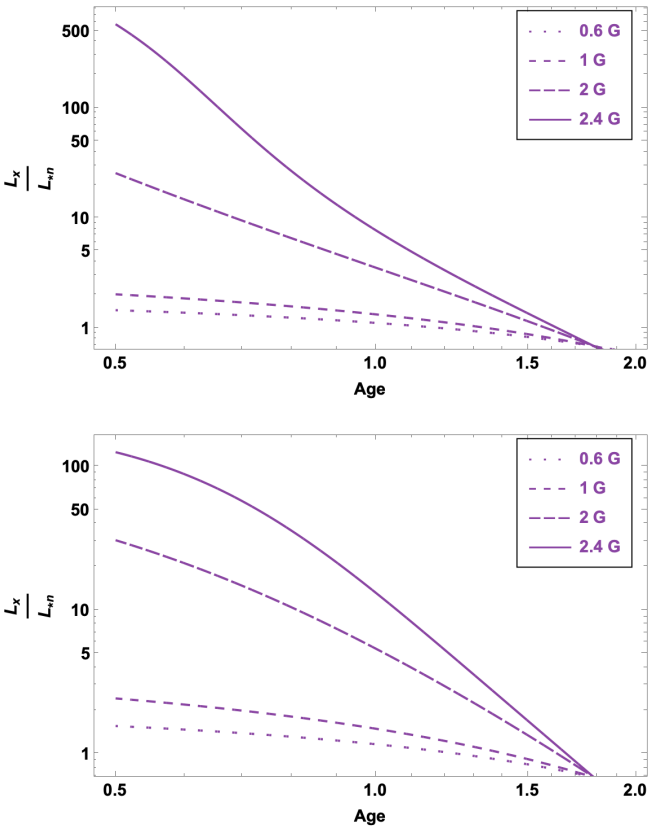

Figure 4. Solutions for l_x versus time for different magnetic field strengths for star 2 form Table 1. This spread in the luminosities further demonstrates the sensitivity of our solutions to surface magnetic field strengths. Here we used the same magnetic field values and line styles as in Fig.3.

for regime I and the bottom panel for regime II using magnetic field values B_p = 0.6 G, 1 G, 2 G, 2.4 G. In both regimes we see the conspicuous difference between solution curves for lower and higher magnetic fields. Fig. 4 demonstrates the influence of magnetic field strength on l_x.

Generally, Figures 3 and 4 show that the broad spread of solutions for the range of magnetic fields considered makes it difficult to predict the exact evolution path for each star. This further highlights the imprecision of any prediction for the population that would arise by using one single-line curve. The theoretical prediction for the population is an envelope of curves.

3.2 Physical role of thermal conduction in Regimes I and II

As mentioned above, we assume that dynamo-produced fields source the coronal energy, which in turn has three main processes for energy loss: stellar wind, thermal conduction and X-ray radiation. The first two increase with increasing temperature, while X-ray radiation decreases. This leads to an equilibrium with a minimum total coronal flux (Hearn 1975). For regime I, thermal conduction and X-ray luminosity dominate the energy loss leaving little contribution from the stellar wind. Here conduction removes hot gas available for the wind and the wind mass-loss rate correspondingly drops exponentially with decreasing gas temperature. This, in turn, reduces the rate of angular momentum loss. In regime II, conduction is sub-dominant and wind loss and X-ray radiation dominate the coronal energy loss.

The difference in increasing and decreasing slope between regimes in our solutions shown in Figure 2 with colored curves is caused by the relative influence of thermal conduction, which is more important at low temperatures where it determines the relation between luminosity and mass loss, and in turn, the coupled evolution of x-ray luminosity, magnetic field strength, and spin.

In the spin evolution model used by van Saders et al. (2016), the scaling between luminosity and mass loss is the same as in our regime II, equation (18), although for different reasons. This may help to explain why their solutions (shown as black dot-dashed line in Figure 2) also have a faster rate of spin down. But their results for the time evolution of the rotation period are quite different from ours due to different parameter choices and a different relation between luminosity and angular velocity. For our case $l_x \sim \omega^3$ for $\lambda = 1/3$ and for their case $l_x \sim \omega^2$.

3.3 Influence of feedback of rotation on magnetic field evolution

In regime I, the relationship between luminosity and mass loss is very different from regime II. As a result the solutions in Figure 2 show a decreasing slope, and are quite similar to the Skumanich relation for older main sequence stars. Regime I overall shows better agreement with the data, although our envelope of solutions using either regime I or regime II can describe the observed period-age relation without requiring a change of a dynamo mode.

That the solutions curves for regime I versus regime II in Fig. 2 are not hugely different can be explained by considering the feedback between the rotation and the magnetic field. For low mass loss (regime I) the change in the angular momentum, and in turn, the magnetic field is insignificant, while for regime II stars are losing angular momentum faster, thereby reducing the magnetic field more than in regime I. Because of the dynamical coupling between the magnetic field and stellar rotation, reducing the magnetic field also reduces the spin-down rate, resulting in a similar rotation period evolution to that of regime.[2]

4 CONCLUSION

To study the time evolution of the stellar rotation period and the period-age relationship for G and F-type main sequence stars we have employed and generalized a minimalist holistic time-dependent model for spin-down, X-ray luminosity, magnetic field, and mass loss (Blackman & Owen 2016). The model combines an isothermal Parker wind (Parker 1958), dynamo saturation model (Blackman & Thomas 2015), a coronal equilibrium condition (Hearn 1975), and assumes that angular momentum is lost primarily from the equatorial plane (Weber & Davis 1967).

From a sample of older-than-solar stars chosen for having precise measurements of period and age, we solved these evolution equations such that each star is a fixed point on a unique solution curve. We argued that the envelope of these curves is a more appropriate indicator of theoretical predictions than a single line fit through the sun or any chosen star to represent the entire population.

We produce separate such envelopes for cases in which thermal conduction is respectively less or more important, with the latter appears to be in better agreement with the data. Overall, our results suggest that a dynamo transition from dipole dominated to higher multipole dominated is not unambiguously required to reduce the

[2] Remember that these stars are in the unsaturated regime, where magnetic field and X-ray luminosity do depend on spin.

Table 1. Stellar properties of G-type and F-type stars used in our study (Wright et al. (2004); Bazot et al. (2012); Molenda-Żakowicz et al. (2013); Marsden et al. (2014); van Saders et al. (2016); Creevey, O. L. et al. (2017); White, T. R. et al. (2017); Metcalfe et al. (2022))

	KIC ID/Name or HIP no.	Sp. Type	Radius ($R_\odot$)	Mass ($M_\odot$)	Age (Gyr)	Period (Days)	Luminosity ($L_\odot$)	Rossby number	Magnetic field (G)
1	Sun	G2V	1.001 ± 0.005	1.001 ± 0.019	4.6	24.47	0.97 ± 0.03	2	2
2	9098294	G3V	1.150 ± 0.003	0.979 ± 0.017	8.23 ± 0.53	19.79±1.33	1.34 ± 0.05		
3	7680114	G0V	1.402 ± 0.014	1.092 ± 0.030	6.89 ± 0.46	26.31±1.86	2.07 ± 0.09		
4	α Cen A	G2V	1.224 ± 0.009	1.105 ± 0.007	5.40 ± 0.30	22±5.9	1.55 ± 0.03		
5	16 Cyg-A	G1.5Vb	1.223 ± 0.005	1.072 ± 0.013	7.36 ± 0.31	$20.5^{+2}_{-1.1}$	1.52 ± 0.05		< 0.5
6	16 Cyg-B	G3V	1.113 ± 0.016	1.038 ± 0.047	7.05 ± 0.63	$21.2^{+1.8}_{-1.5}$	1.21 ± 0.11		< 0.9
7	18 Sco	G2Va	1.010 ± 0.009	1.020 ± 0.003	$3.66^{+0.44}_{-0.5}$	22.7 ± 0.5	1.07 ± 0.03		1.34
8	1499	G0V	1.11 ± 0.04	$1.026^{+0.04}_{-0.03}$	$7.12^{+1.40}_{-1.56}$	$29^{+0.3}_{-0.3}$	1.197	2.16	0.6 ± 0.5
9	682	G2V	1.12 ± 0.05	$1.045^{+0.028}_{-0.024}$	$6.12^{+1.28}_{-1.48}$	$4.3^{+0.0}_{-0.2}$	1.208	0.4	4.4 ± 1.8
10	1813	F8	$1.18^{+0.06}_{-0.05}$	$0.965^{+0.02}_{-0.02}$	$10.88^{+1.36}_{-1.36}$	$22.1^{+0.2}_{-0.2}$	1.315	1.95	2.4 ± 0.7
11	176465 A	G4V	0.918 ± 0.015	0.930 ± 0.04	3.0 ± 0.4	19.2±0.8			
12	176465 B	G4V	0.885 ± 0.006	0.930 ± 0.02	2.9 ± 0.5	17.6±2.3			
13	400	G9V	$0.8^{+0.02}_{-0.03}$	$0.794^{+0.034}_{-0.018}$	$12.28^{+1.72}_{-7.08}$	$35.3^{+1.1}_{-0.7}$	0.455	2	2.1 ± 1.0
14	6116048	F9IV-V	1.233 ± 0.011	1.048 ± 0.028	6.08 ± 0.40	17.26±1.96	1.77 ± 0.13		
15	3656476	G5IV	1.322 ± 0.007	1.101 ± 0.025	8.88 ± 0.41	31.67±3.53	1.63 ± 0.06		

[a] For 16 Cyg-A 16 Cyg-B and 18 Sco we used estimated mass loss rates from Metcalfe et al. (2022), based on the scaling relation $\dot{M} \simeq F_x^{0.770.04}$ (Wood et al. 2021). For other stars we have used the Solar value.
[*] In our solutions we have used Solar values for these parameters.

rate of spin down, as there is not a clear contradiction between theory and observation for the envelope of solutions without such a transition when the theory depends on a Parker-type wind solution.

We explored the sensitivity of our solutions to stellar properties that we may not know for individual stars, such as the coronal base X-ray temperature and magnetic field strength. Because the Parker-type wind solution is integral to the model, we are forced to an exponential sensitivity on the coronal base X-ray temperature. This limits the precision of any theoretical or model prediction expressed as a single line intended to capture the evolution of the stellar population. The prediction should instead be expressed as an envelope of curves. Said another way, the sample of observed data does not have enough sufficiently identical stars to make an ensemble average prediction of high precision. This connects to the broader need to more commonly express limitations in precision of theory field theories applied to astrophysical systems (Zhou et al. 2018).

Since it is not possible to obtain more than 1 data point for individual stars over their spin-down evolution lifetimes, more observations to better nail down evidence for or against a spin-down transition are desired. More data on individual more closely "identical" stars at different times in their spin-down evolution would be desirable. In addition, at the population level, period-mass plots for older clusters than have presently been measured would be valuable. Observations from the Kepler K2 mission have shown that by the time clusters reach an age of 950Myr, period-mass relations appear to converge to a relatively tight 1 to 1 dependence Godoy-Rivera et al. (2021). Similar results were obtained for 2.7 Gyr-old open cluster Ruprecht 147 (Gruner & Barnes 2020), who found that stars lie in period-mass-age plane with possible evidence for a mass dependence requiring additional mass-dependent physics parameter variation (perhaps e.g. relating to our q below Eqn. 10 deviating from unity), in modeling spin-down. If similar data could be obtained for much older clusters and the tight relations were to show strong kinks or bifurcate into more than one branch within the mass range $0.5 < M/M_\odot < 1.5$ that we have considered, this would suggest that the population of solar-like stars that we are focusing on would show population-level evidence for a transition.

5 DATA AVAILABILITY

All the data used in the paper is either created theoretically from equations herein, or given in Table 1.

6 ACKNOWLEDGMENTS

KK acknowledges support from a Horton Graduate Fellowship from the Laboratory for Laser Energetics. We acknowledge support from the Department of Energy grants DE-SC0020432 and DE-SC0020434, and National Science Foundation grants AST-1813298 and PHY-2020249. EB acknowledges the Isaac Newton Institute for Mathematical Sciences, Cambridge, for support and hospitality during the programme "Frontiers in dynamo theory: from the Earth to the stars"where work on this paper was undertaken. This work was supported by EPSRC grant no EP/R014604/1. JEO is supported by a Royal Society University Research Fellowship. This work was supported by the European Research Council (ERC) under the European Union's Horizon 2020 research and innovation programme (Grant agreement No. 853022, PEVAP). For the purpose of open access, the authors have applied a Creative Commons Attribution (CC-BY) licence to any Author Accepted Manuscript version arising.

REFERENCES

Bazot M., Bourguignon S., Christensen-Dalsgaard J., 2012, Monthly Notices of the Royal Astronomical Society, 427, 1847
Blackman E. G., Brandenburg A., 2003, ApJ, 584, L99
Blackman E. G., Field G. B., 2002, Physical Review Letters, 89, 265007
Blackman E. G., Owen J. E., 2016, MNRAS, 458, 1548
Blackman E. G., Thomas J. H., 2015, MNRAS, 446, L51
Cranmer S. R., 2004, American Journal of Physics, 72, 1397

Creevey, O. L. et al., 2017, A&A, 601, A67
Gallet F., Bouvier J., 2013, Astronomy & Astrophysics, 556, A36
Godoy-Rivera D., Pinsonneault M. H., Rebull L. M., 2021, ApJS, 257, 46
Gough D. O., 1981, Sol. Phys., 74, 21
Gruner D., Barnes S. A., 2020, A&A, 644, A16
Hearn A. G., 1975, Astron. & Astrophys., 40, 355
Johnstone C. P., Güdel M., Brott I., Lüftinger T., 2015, A&A, 577, A28
Kawaler S. D., 1988, ApJ, 333, 236
Lamers H. J. G. L. M., Cassinelli J. P., 1999, Introduction to Stellar Winds. Cambridge Univ. Press
Mamajek E. E., 2014, Figshare, http://dx.doi.org/10.6084/m9.figshare.1051826
Marsden S. C., et al., 2014, MNRAS, 444, 3517
Matt S. P., MacGregor K. B., Pinsonneault M. H., Greene T. P., 2012, ApJ, 754, L26
Matt S. P., Brun A. S., Baraffe I., Bouvier J., Chabrier G., 2015, ApJ, 799, L23
Mestel L., 1968, Monthly Notices of the Royal Astronomical Society, 138, 359
Metcalfe T. S., van Saders J., 2017, Solar Physics, 292, 1
Metcalfe T. S., et al., 2022, The Astrophysical Journal Letters, 933, L17
Molenda-Żakowicz J., et al., 2013, Monthly Notices of the Royal Astronomical Society, 434, 1422
Nichols-Fleming F., Blackman E. G., 2020, MNRAS, 491, 2706
Parker E. N., 1955, ApJ, 122, 293
Parker E. N., 1958, ApJ, 128, 664
Peres G., Orlando S., Reale F., Rosner R., Hudson H., 2000, ApJ, 528, 537
Reiners A., Mohanty S., 2012, The Astrophysical Journal, 746, 43
Reiners A., Schüssler M., Passegger V. M., 2014, ApJ, 794, 144
Schatzman E., 1962, Annales d'Astrophysique, 25, 18
Skumanich A., 1972, ApJ, 171, 565
Steenbeck M., Krause F., 1969, Astronomische Nachrichten, 291, 49
Weber E. J., Davis Jr. L., 1967, ApJ, 148, 217
White, T. R. et al., 2017, A&A, 601, A82
Wood B. E., et al., 2021, The Astrophysical Journal, 915, 37
Wright J. T., Marcy G. W., Butler R. P., Vogt S. S., 2004, The Astrophysical Journal Supplement Series, 152, 261
Wright N. J., Drake J. J., Mamajek E. E., Henry G. W., 2011, ApJ, 743, 48
Zhou H., Blackman E. G., Chamandy L., 2018, Journal of Plasma Physics, 84, 735840302
van Saders J. L., Pinsonneault M. H., 2013, ApJ, 776, 67
van Saders J. L., Ceillier T., Metcalfe T. S., Silva Aguirre V., Pinsonneault M. H., García R. A., Mathur S., Davies G. R., 2016, Nature, 529, 181

This paper has been typeset from a TEX/LATEX file prepared by the author.